NeuroImage 277 (2023) 120210

Contents lists available at ScienceDirect

NeuroImage

journal homepage: www.elsevier.com/locate/neuroimage

Diffuse optical tomography spatial prior for EEG source localization in human visual cortex

Jiaming Cao[a], Eli Bulger[a], Barbara Shinn-Cunningham[a,b,c,d], Pulkit Grover[a,b,c], Jana M Kainerstorfer[a,b,c,*]

[a] Department of Biomedical Engineering, Carnegie Mellon University, 5000 Forbes Avenue, Pittsburgh, 15213, Pennsylvania, United States
[b] Department of Electrical and Computer Engineering, Carnegie Mellon University, 5000 Forbes Avenue, Pittsburgh, 15213, Pennsylvania, United States
[c] Neuroscience Institute, Carnegie Mellon University, 4400 Fifth Avenue, Pittsburgh, 15213, Pennsylvania, United States
[d] Department of Psychology, Carnegie Mellon University, 5000 Forbes Avenue, Pittsburgh, 15213, Pennsylvania, United States

ARTICLE INFO

Keywords:
Electroencephalography
Diffuse optical tomography
Spatio-temporal resolution
Source reconstruction

ABSTRACT

Electroencephalography (EEG) and diffuse optical tomography (DOT) are imaging methods which are widely used for neuroimaging. While the temporal resolution of EEG is high, the spatial resolution is typically limited. DOT, on the other hand, has high spatial resolution, but the temporal resolution is inherently limited by the slow hemodynamics it measures. In our previous work, we showed using computer simulations that when using the results of DOT reconstruction as the spatial prior for EEG source reconstruction, high spatio-temporal resolution could be achieved. In this work, we experimentally validate the algorithm by alternatingly flashing two visual stimuli at a speed that is faster than the temporal resolution of DOT. We show that the joint reconstruction using both EEG and DOT clearly resolves the two stimuli temporally, and the spatial confinement is drastically improved in comparison to reconstruction using EEG alone.

1. Introduction

Electroencephalography (EEG) is a neuroimaging method, which is sensitive to the electrical activities of neurons. It has been one of the most commonly used techniques for neural monitoring due to its high sample rate, ease of operation, and bedside compatibility. Knowing where the neuronal activation occurs can be crucial, for instance, for localizing epileptic foci (Michel and He, 2019). In order to identify where activation is occurring, source localization algorithms need to be applied. Although the temporal resolution of EEG can be very high (several kilohertz), the spatial resolution is typically limited (a few centimeters), especially when low-density systems are used (Grover and Venkatesh, 2017).

In order to improve the spatial accuracy of EEG source localization, information about where the activation occurs, often referred to as spatial priors, can be used. This can be achieved by simultaneous recording of functional magnetic resonance imaging (fMRI). While the temporal resolution of fMRI is inherently limited by the nature of the hemodynamics that it measures (on the order of 10 s Keles et al., 2016), the spatial resolution is very high (mm-scale). Despite the differences in the specific assumptions and implementations, most of the algorithms are based on the same basic assumption (Ferdowsi et al., 2015; Henson et al., 2010; Liu and He, 2008; Oberlin et al., 2015): neuronal and hemodynamic activities are closely coupled and co-localized. The high-resolution spatial information from fMRI can therefore be used to inform and spatially confine the EEG reconstruction. It has been shown in both simulations and experiments that EEG-fMRI fusion algorithms can achieve spatio-temporal reconstruction of neuronal activities (Liu and He, 2008). While fMRI can improve spatial resolution of source localization, combined measurements can be difficult because some subjects may not be fMRI-compatible e.g. those with implants. Moreover, that the experiments have to be conducted within an fMRI machine makes it infeasible to have bedside or long-term measurements.

As an alternative to fMRI, diffuse optical tomography (DOT) can be used to obtain spatial priors from the cerebral cortex. DOT is an optical imaging method that, similar to fMRI, reconstructs the hemodynamic responses in the brain, and has seen a rapid increase in popularity in recent years. Particularly, a commonly-used continuous-wave DOT system, which is used in this study, reconstructs the changes of oxy- and deoxy-hemoglobin (changes of HbO and Hb, or ΔHbO and ΔHb for short, respectively) with regard to baseline. It has been shown that fMRI-comparable spatial resolution can be achieved when using a high-density system (Eggebrecht et al., 2012), and various recent neonatal and clinical applications (Ayaz et al., 2022) indicate that the DOT technology is quickly maturing. In comparison to fMRI, DOT has the ben-

* Corresponding author.
E-mail addresses: jiamingc@andrew.cmu.edu (J. Cao), jkainers@andrew.cmu.edu (J.M. Kainerstorfer).

https://doi.org/10.1016/j.neuroimage.2023.120210.
Received 27 April 2023; Accepted 30 May 2023
Available online 11 June 2023.

efits of being relatively low-cost, compatible with subjects with metal implants, and portable. We therefore explored feasibility of using DOT in place of fMRI to derive spatial priors for EEG reconstruction.

Indeed, work has been done to improve EEG source reconstruction using simultaneously recorded functional near-infrared spectroscopy (fNIRS) (Aihara et al., 2012), which is based on the same physical principles as DOT. A key limitation of this method is that when using fNIRS, the spatial prior was derived by projecting the hemodynamic responses onto the brain surface instead of obtained by solving an inverse problem as is used in DOT. We showed in our previous work (Cao et al., 2021) that the spatial accuracy of projection is much lower than that of the solution to the inverse problem, and the improvement of EEG reconstruction is therefore inferior.

In our previous work (Cao et al., 2021), we proposed a method that utilizes the reconstruction results from simultaneously recorded DOT as the spatial prior to improve the spatial accuracy of EEG. We showed, using computer simulations on a realistic head model, that high-resolution spatio-temporal reconstruction of neuronal sources could be achieved, and the improvement was more drastic than the fNIRS projection-based method (Aihara et al., 2012).

In this work, we experimentally validated the previously proposed EEG-DOT combination algorithm by showing that two sequentially activated brain regions can be resolved both spatially and temporally with better accuracy than using either of the two modalities alone. In particular, we displayed a checkerboard wedge at two locations alternatingly and record EEG and DOT simultaneously. The use of a checkerboard wedge at two different locations as the visual stimulus is derived from the conventional retinotopic mapping experiments done in the DOT as well as fMRI field (White and Culver, 2010a; Zeff et al., 2007), which are well-known to evoke strong hemodynamic responses in the visual cortex. According to the retinotopy theory, displaying the checkerboard wedge at two locations will activate two different corresponding brain regions on opposite hemispheres in occipital cortex (Zeff et al., 2007). While using EEG alone can distinguish between the two stimulus locations, it is difficult to accurately estimate the spatial content of the activated brain region, because the large point spread of EEG will likely overestimate it. The rate at which the two stimuli alternate was chosen to be fast enough, such that when the two brain regions are alternatingly activated, our DOT alone does not have the sufficient temporal resolution to *reliably* differentiate them (see Section 4). Therefore, the experiment design allows us to demonstrate the effectiveness of our EEG-DOT joint source reconstruction algorithm by showing a) the two activated brain regions can be temporally resolved, and b) spatially, the activated brain regions can be reconstructed with better confinement. In the following sections, we first describe the experiment protocol in detail and briefly explain the joint reconstruction algorithm. After that, we present the results of reconstruction using only EEG, only DOT, and EEG with DOT-derived prior, and show the improved spatio-temporal resolution achieved by using the EEG-DOT joint source reconstruction algorithm. Finally, we discuss some potential drawbacks of the method as well as future directions.

2. Methods

2.1. Experiment protocol

The study was approved by the Institutional Review Board of Carnegie Mellon University (STUDY2019_00000021). Nineteen healthy volunteers participated in the experiments, which is close to the number of subjects used in classic literature (Eggebrecht et al., 2014). A 45-degree-wide black-and-white checkerboard wedge was displayed alternatingly on the left- and right-hand side (stimulus “A” and “B”, as is illustrated in Fig. 1(a)) of the bottom half of a 24-inch monitor on a 50% gray background. A crosshair was also displayed at the center of the monitor, and the subjects were asked to fixate the center of their visual field on the crosshair. The subjects were seated in a dark room 80 cm away from the monitor, with each checkerboard extending to a visual angle of approximately 8 degrees from fixation, consistent with the typical values reported in the literature (White and Culver, 2010a).

The experimental protocol followed a block design (see Fig. 1(b) for illustration). Particularly, one block was 35 s long, consisting of 10 s of fixation on a blank (except for the fixation crosshair) gray screen, followed by 15 s of stimuli and another 25 s of fixation on a blank gray screen for the hemodynamics to fully reset. A gray screen was displayed between the blocks, and the pause periods were manually terminated by the subjects through keyboard interaction. During the stimulation period, each of the checkerboard positions was displayed for 200 ms, with a 175 ms stimulus-off period in between. The sequence of “stimulus A - blank - stimulus B - blank” was considered as one trial, and the trial was repeated continuously for 20 times in each block, which formed the above-mentioned 15-second stimulation period. The inter-stimulus interval for each stimulus (A or B) was effectively 550 ms. The block was repeated 25 times for each subject except for Subject 1 and Subject 9. Subject 1 underwent 15 blocks due to time constraints, and Subject 9 underwent 13 blocks because of a hardware issue.

While the stimuli are similar to those used in the eccentricity experiment in (Zeff et al., 2007), the checkerboard wedges were chosen to be displayed in a fast alternating pattern, such that DOT alone does not have enough temporal resolution to distinguish between the two locations. In addition, while EEG reconstruction can distinguish between the two locations (see Section 3), the spatial accuracy (in terms of the spread of spatial extent) would still be low because only 64 electrodes were used in the experiment (see Section 2.2 for the hardware setup). According to literature (Grover and Venkatesh, 2017), the point spread of a 64-channel EEG system is on the order of several centimeters.

2.2. Data acquisition

DOT was recorded using a continuous-wave NIRSport 2 system (NIRx, Medical Technologies, LLC), sampling at 5.1 Hz. A total of 24 sources and 21 detectors were used, forming 76 channels that covered primarily the visual cortex and the adjacent regions (Fig. 2). For each DOT source, two wavelengths, namely 760 nm and 850 nm were used. The DOT grid has an average source-detector separation of 2.7 cm. Except for Subjects 1 and 2, three-dimensional accelerometer and gyroscope data were simultaneously recorded using the built-in sensor of the NIRSport 2 device, with the sensor placed close to the Cz location.

EEG was simultaneously recorded using an ActiveTwo system (BioSemi B.V., Amsterdam, Netherlands), sampling at 2048 Hz. We used 64 channels to measure the whole head, following the standard 10-10 locations (Oostenveld and Praamstra, 2001). All the DOT optode holders and EEG electrode holders were installed on the same BioSemi cap, and the layout of the cap is illustrated in Fig. 2(b).

2.3. Forward modeling

For both EEG and DOT, the forward model was assumed to have the linear form,

$$\mathbf{y} = \mathbf{A}\mathbf{x} + \boldsymbol{\epsilon} \tag{1}$$

where $\mathbf{y}$ is the measurement vector, $\mathbf{A}$ is the forward matrix, $\mathbf{x}$ is the brain activity vector, and $\boldsymbol{\epsilon}$ is the measurement noise.

To generate the EEG forward model, the standard model consisting of scalp, skull, and brain layers available in the Fieldtrip toolbox, which is based on the Colin27 model (Oostenveld et al., 2011; 2003), was used. In the triangularized boundary elementy model (BEM), there were 500, 1000, 1500 nodes, and 996, 1996, 1996 triangles in the three layers respectively. The 8196 neuronal sources were chosen to be at the standard locations defined in Fieldtrip, which is also based on the Colin27 model (Oostenveld et al., 2011; 2003). The same toolbox was used to compute the forward matrix, where the resistivities of the three layers were assumed to be 1:80:1 (Grover and Venkatesh, 2017).

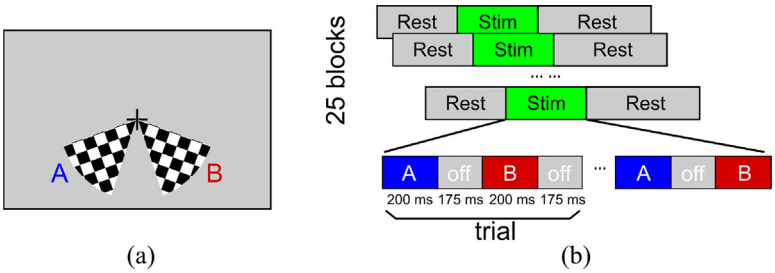

Fig. 1. (a) An illustration of the visual stimuli used in the experiments. The two checkerboard wedges A and B were displayed alternatingly. (b) An illustration of the block design.

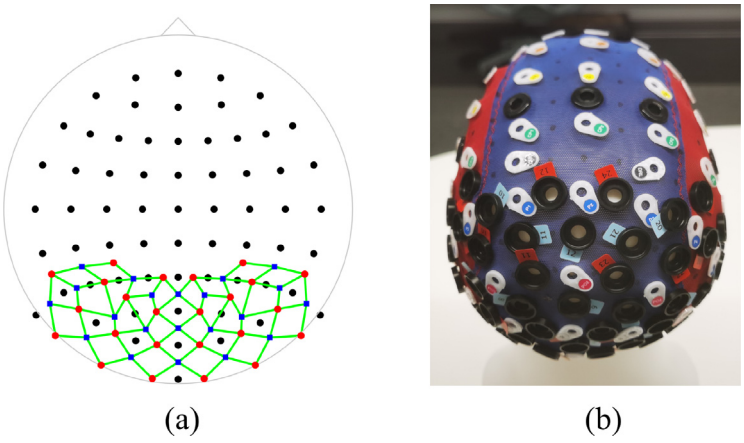

Fig. 2. The configuration of DOT and EEG used in the experiments. (a) A 2D illustration of the setup. Black dots: EEG electrodes; red dots: DOT sources; blue dots: DOT detectors; green lines, DOT channels. (b) The cap used in the experiments mounted on a mannequin. White rings: BioSemi EEG electrode holders; black rings in the back: NIRx optode holders; black rings in the middle: locations where the accelerometer and the cable organizers were installed. (For interpretation of the references to colour in this figure legend, the reader is referred to the web version of this article.)

The same segmented head model was converted to a solid tetrahedral mesh using the iso2mesh toolbox (Fang and Boas, 2009), forming 189,274 nodes and 1,177,487 tetrahedrons in total. The tetrahedral mesh was then loaded into the NIRFASTer toolbox (Dehghani et al., 2009), where a finite element model (FEM) was used to compute the standard forward matrix (i.e. optical density changes resulting from the absorption coefficient changes of the neuronal sources) of the DOT system, where the optical properties of the three layers were chosen according to Eggebrecht et al. (2012). Finally, the desired forward model was constructed by,

$$\mathbf{A}_{DOT} = \begin{pmatrix} \mathbf{J}_{760} \cdot \xi_{HbO,760} & \mathbf{J}_{760} \cdot \xi_{Hb,760} \\ \mathbf{J}_{850} \cdot \xi_{HbO,850} & \mathbf{J}_{850} \cdot \xi_{Hb,850} \end{pmatrix} \tag{2}$$

where $\mathbf{J}_{760}$ and $\mathbf{J}_{850}$ are the standard forward matrices at the two wavelengths, and $\xi_{c,\lambda}$'s are the extinction coefficients of chromophore c at wavelength λ. The final forward model therefore linearly relates the sensor-space optical density changes to the hemoglobin changes in the brain.

2.4. Data preprocessing

The EEG data was re-referenced to the average of the two mastoid channels, bandpass filtered between 1 and 50 Hz, and downsampled to 256 Hz. Independent component analysis (ICA) was performed to reject the components related to eye-blinking artifacts, which were defined as the components highly correlated (Pearson correlation greater than 0.4) with the average of channels Fp1, Fp2, and Fpz. The approximation was empirically determined to effectively remove the eye blinking artifacts. Bad electrodes were defined as those that had excessive standard deviation (greater than 50 μV), and they were repaired by interpolating using the neighboring electrodes. The number of bad electrodes that needed to be repaired ranged from 0 to 9, with an average of 1.3 per subject. The neighboring electrodes were defined according to the default of the Fieldtrip toolbox. PCA filter (Santosa et al., 2018) was applied to filter out remaining noise and interference noise from DOT while preserving the evoked potentials. The first principle component was removed for all subjects except for Subject 16, where the first seven principle components were removed to sufficiently remove the noise. The data was then divided into epochs that started from 50 ms before the onsets of the trials (see Section 2.1) until 750 ms after, totaling 800 ms. Epochs with any channel having high amplitudes (100 μV) were rejected. Finally, average epochs were calculated across all trials of all the subjects.

The DOT data was first converted to optical density changes (ΔOD) and detrended using a 2nd order polynomial. After that, the temporal derivative distribution repair (TDDR) algorithm (Fishburn et al., 2019) was applied to remove the motion artifacts. A moving window of 6 s was then used to remove the remaining motion artifacts. Specifically, if the summation of the absolute values of the temporal differential in a window was high, the data in the window was replaced with a straight line connecting the starting point the and the ending point of the window. The data was then highpass filtered above 0.01 Hz, and further fitted to a generalized linear model (GLM), where the design matrix consisted of a linear trend regressor, a constant bias regressor, a regressor of interest constructed by convolving the stimuli with the canonical hemodynamic response function used in SPM12 toolbox), and the motion artifact regressors. In subjects 1 and 2, the motion artifact regressor was approximated by the average of all the optical density measures, and in all other subjects, it was chosen to be the three-dimensional data from both the accelerometer and the gyroscope which was filtered above 0.01 Hz, totaling six regressors. The GLM model was then solved using an autoregression-iteratively reweighted least square (AR-IRLS) method (Barker et al., 2013) to reduce the impact of artifacts in the data.

2.5. Reconstruction

When performing EEG reconstruction, Tikhonov regularization was applied to each time point of the averaged epoch, where the regularization coefficient was chosen to be 5e-8 using the L-curve method (Grech et al., 2008).

Before performing DOT reconstruction, the signal quality of each channel was estimated. Specifically, heart rate was first estimated as

the strongest frequency component between 0.8 and 1.5 Hz. After that, for each channel, the signal-to-noise ratio (SNR) was estimated by dividing the spectral power around the heart rate (±0.1 Hz) by the spectral power around 1.5 times the heart rate (±0.1 Hz). Only the 850 nm signal was used because it is more sensitive to cardiac pulsations. Finally, a spatially variant Tikhonov regularization was applied to the beta values that resulted from the GLM fitting for each subject using only the "good channels, which were defined as those with SNR above 1.5. The method solves the following optimization problem,

$$\arg\min_{\mathbf{x}} ||\mathbf{y}-\mathbf{A}\mathbf{x}||_2^2+\alpha||\mathbf{L}\mathbf{x}||_2^2 \tag{3}$$

where $\mathbf{L}$ is a diagonal matrix with,

$$\mathbf{L}=\sqrt{\mathbf{A}^T\mathbf{A}+\beta} \tag{4}$$

α and β are the hyperparameters, and were chosen to be $\alpha=0.01$ and $\beta=0.1$ respectively according to Eggebrecht et al. (2014).

After performing reconstruction of ΔHbO and ΔHb during the visual stimulation for each individual subject, the group averaged reconstruction was then calculated. Subjects 4, 9, and 15 were excluded from the group average due to excessive amounts of noise (more than 30 channels were noisy according to the previously mentioned SNR criteria).

In order to demonstrate the improvement of EEG reconstruction with DOT, the algorithm proposed in our previous work (Cao et al., 2021) was used. Briefly, the algorithm makes the assumption that a brain voxel should *only* have high electrical activity (reconstructed from EEG) when the hemodynamic activity (reconstructed from DOT) is high. In particular, the algorithm attempts to solve the following restricted maximum likelihood (ReML) problem,

$$\arg\max_{\mathbf{x},\mathbf{C}_\mathrm{N},\mathbf{C}_\mathrm{P}} -||\mathrm{Y}-\mathbf{A}\mathbf{x}||^2_{\mathbf{C}_\mathrm{N}^{-1}}-||\mathbf{x}||^2_{\mathbf{C}_\mathrm{P}^{-1}}-\log|\mathbf{C}_\mathrm{N}|-\log|\mathbf{C}_\mathrm{P}| \tag{5}$$

where $\mathbf{C}_N$ denotes the covariance matrix of measurement noise, $\mathbf{C}_P$ denotes the covariance matrix of the prior distribution of the neuronal sources, and for some arbitrary matrices $\mathbf{X}$ and $\mathbf{M}$, the notation $||\mathbf{X}||_\mathbf{M}$ denotes the weighted norm: $||\mathbf{X}||^2_\mathbf{M}=\mathbf{X}^T\mathbf{M}\mathbf{X}$.

The measurement noise was assumed to be independent and identically distributed (i.i.d.), i.e. $\mathbf{C}_N\propto\mathbf{I}$, where $\mathbf{I}$ is an identity matrix with the dimensionality of the number of electrodes. To incorporate the DOT reconstruction as the spatial prior for EEG, the reconstructed HbO was first normalized between 0 and 1 by,

$$\mathbf{x}'=\frac{|\hat{\mathbf{x}}_{HbO}|}{\max|\hat{\mathbf{x}}_{HbO}|} \tag{6}$$

where $\hat{\mathbf{x}}_{HbO}$ denotes the reconstructed HbO changes. After that, we incorporated the assumption that one voxel may have strong electrical activities if and only if the hemodynamic responses are strong by imposing the following constraint on the neuronal source covariance matrix,

$$\mathbf{C}_{P\{i,i\}}\propto 1-\exp\left(-\frac{\mathbf{x}'_i+a}{b}\right) \tag{7}$$

where the subscript i denotes the ith element, a and b are scalar constants controlling how strongly the DOT prior affects the EEG reconstruction. In this paper, they were empirically chosen to be 0.1 and 1. A detailed discussion of the algorithm and the parameter selection can be found in our previous work (Cao et al., 2021).

The problem was then solved at each time step of the averaged EEG trial for each subject, with each time step using the same DOT prior. The EEG reconstruction results were then averaged across all subjects except for the three with excess DOT noise. Note that only ΔHbO is used, because it typically has higher SNR than ΔHb (Abdelnour et al., 2010).

In our previous work (Cao et al., 2021), we showed using simulation that while it is possible to use fNIRS projection as the spatial prior to improve EEG source reconstruction, as is done in (Aihara et al., 2012), the improvement is less substantial and can be insufficient. To validate the simulation result using real data, we first calculated the projection of ΔHbO on the cortical surface. Specifically, the same preprocessing pipeline described in Section 2.4 was followed until the highpass filtering, after which the filtered ΔOD was converted into ΔHbO and ΔHb using the modified Beer-Lambert law for each channel. The calculated ΔHbO was then fitted to the same GLM used in Section 2.4, the result of which was projected onto the cortical surface using the method detailed in our simulation study (Cao et al., 2021). Finally, EEG source reconstruction with ΔHbO projection prior was performed using the same pipeline described above, with the only exception that $\hat{\mathbf{x}}_{HbO}$ in this case denotes the projected activity, instead of the reconstruction.

3. Results

The group average of the DOT reconstruction is shown in Fig. 3. One-sided t-test (mean greater than zero and mean less than zero for ΔHbO and ΔHb) was performed for each voxel. The results with and without p-value masking ($p<0.05$) are shown in the first and second row, respectively. An increase of HbO and a decrease of Hb can be observed in the middle and superior occipital cortex, agreeing with the expected response locations given the stimuli used in this study (Ferradal et al., 2014; White and Culver, 2010a) (highlighted in green boxes). Note that the reconstructed changes of Hb are weaker on the right hemisphere. This can be because of the relatively low SNR of ΔHb, which is a well-known property of Hb, making it difficult to reconstruct in general (Abdelnour et al., 2010).

The improvement of spatial accuracy of EEG source reconstruction when using the DOT-derived spatial prior is illustrated at the respective N170 peaks of stimuli A and B in Fig. 4. Particularly, shown in the figure are the group-averaged reconstruction results of the individual subjects. Two-sided t-test was performed for each voxel to test if the reconstructed activity is non-zero. For all the subfigures in Fig. 4, only voxels with $p<0.05$ are shown. The N170 peaks were chosen because, in this experiment, these are the time points where the strongest EEG activation was observed, as is shown in Fig. 5, where the group average time traces of three EEG channels, namely PO3, POz, and PO4, are shown. They are chosen because PO3 and PO4 are approximately above the active regions in response to stimuli A and B, and POz is in the middle equally picking up responses from both stimuli. Reconstruction results in comparison to the standard AAL brain atlas (Rolls et al., 2020) are shown in Supplementary Fig. S2. Comparison between EEG reconstruction results with and without DOT prior at various time points can be found in Supplementary Fig. S4. Videos showing the full process of the reconstructed visual responses with and without DOT prior can also be found in Supplementary materials.

The results of ΔHbO projection onto the cortical surface is shown in Fig. 6. One-sided t-test was performed at each voxel to test if the mean is greater than zero. It can be seen that in comparison to Fig. 3(a) and (c), the inferred active regions are largely the same, but the spatial spread of projection is much larger, spreading into parietal lobe, where activation is not expected.

The improvement of spatial accuracy of EEG source reconstruction when using the ΔHbO projection prior is illustrated at the respective N170 peaks of stimuli A and B in Fig. 7. The same two-sided t-test described above was also performed. Improved confinement of the spatial content when using the prior can be observed, but much less substantial in comparison to the results shown in Fig. 4. This is to be expected because the projection-based spatial prior has greater spatial spread in comparison to the reconstruction-based prior, and the less substantial decrease in sptatial spread is consistent with our simulation results (Cao et al., 2021). Reconstruction results are localized to middle and superior occipital cortex in comparison to the standard brain atlas, which is shown in Supplementary Fig. S3.

The improvement spatial accuracy can be further quantitatively compared using a spread metric, which is defined as the radius of the smallest ball that centers at a given center point, and contains all the voxels whose amplitudes are above (in absolute value) half of the highest amplitude. In this paper, we picked the center to be the center of mass of

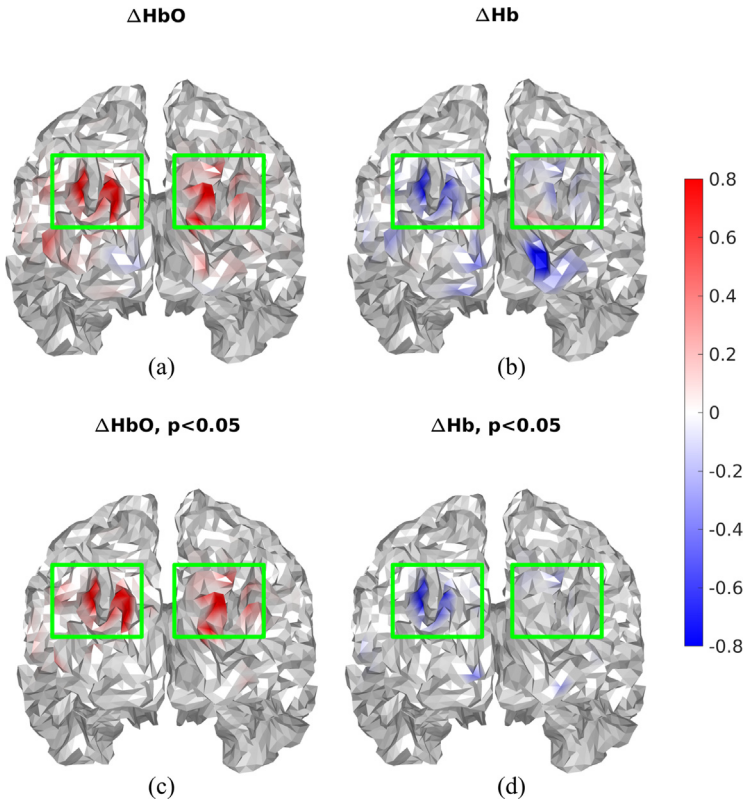

Fig. 3. Group average of the reconstructed HbO and Hb activation, normalized between -1 and 1. Colorbars slightly saturated for better visualization. The green boxes roughly indicate the regions where strong activity is expected to be observed according to retinotopy theory. First row: plain group average. Second row: only voxels with $p < 0.05$ are displayed. The standard Colin27-based brain surface from Fieldtrip is used. (For interpretation of the references to colour in this figure legend, the reader is referred to the web version of this article.)

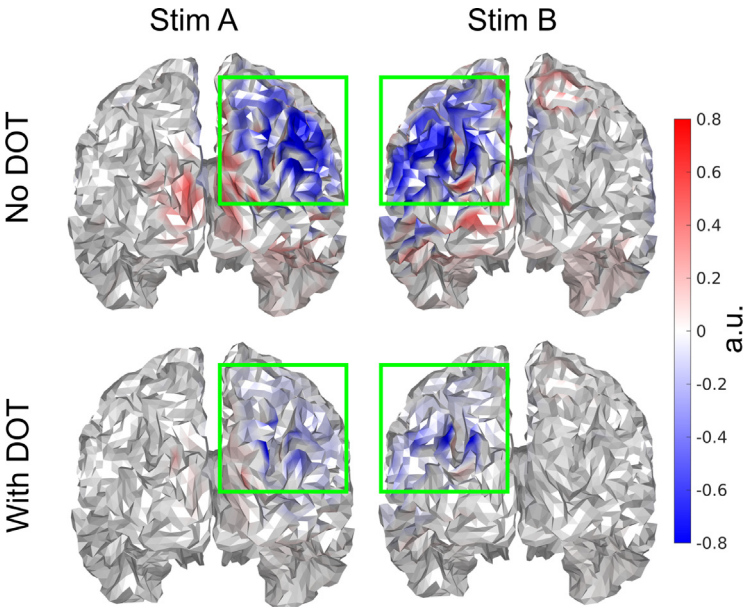

Fig. 4. Improved spatial confinement of source reconstruction at the respective N170 peaks when using DOT as the spatial prior. Each subfigure was individually normalized between -1 and 1 for better clarity. Colorbars slightly saturated for better visualization. Only voxels with $p < 0.05$ are displayed. The standard Colin27-based brain surface from Fieldtrip is used.

the left and right hemispheres (for stimulus B and stimulus A, respectively) calculated using the p-value masked ΔHbO reconstruction. The comparison of the group-level spread (mean and standard deviation) is shown in Fig. 8. One-sided paired t-test was performed to test if there is on average a decrease of spread when using a spatial prior. It can be seen that for both stimuli, the decrease of spatial spread using reconstruction-based DOT prior is more substantial, which is also reflected in the calculated p-values. This is especially true for stimulus B, in which case the null hypothesis that the average spread metric is the same with and without projection-based prior could not be rejected at level 0.05. The results of statistical testing also agree with the qualitative observations that can be made in Figs. 4 and 7. This suggests that while projection-based spatial priors can improve the spatial confinement of EEG source reconstruction, there are still cases where they are insufficient, agreeing with the results shown in our simulation work (Cao et al., 2021).

4. Discussion

This work is the first experimental validation of our previously proposed high spatio-temporal resolution neuronal activity reconstruction algorithm, showing that by using DOT reconstruction as the spatial prior, the spatial accuracy of EEG reconstruction can be substantially

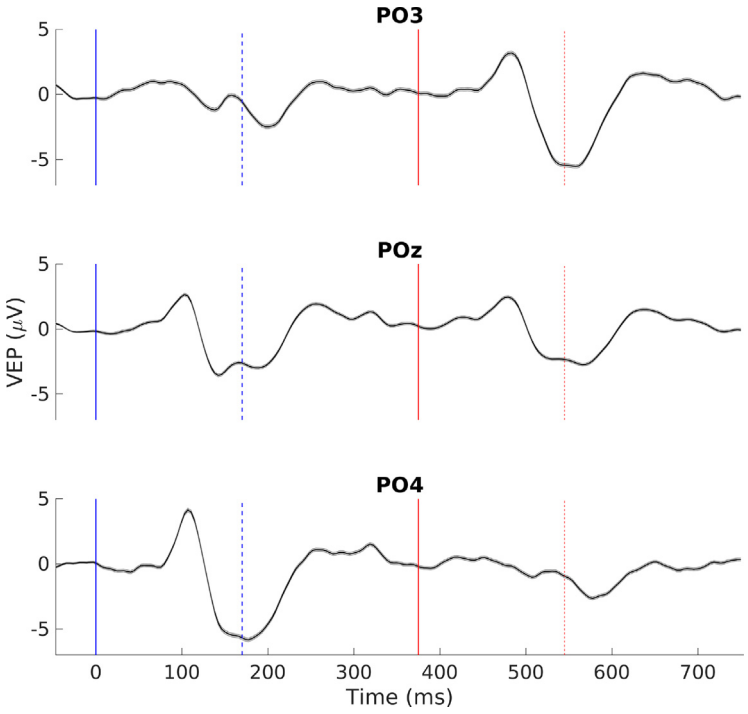

Fig. 5. Group average time traces at EEG channels PO3, POz, and PO4. Error bars indicate the standard errors. The blue and red solid lines indicated the start of stimuli A and B, and the dashed lines indicate the respective N170 peaks. It can be observed that PO3, which is on the left hemisphere, shows strong response to stimulus but barely any response to stimulus A, and vice versa for PO4. POz, which is in the middle, responds equally to both stimuli, albeit with lower amplitude due to the greater distance from the centers of neuronal activity. (For interpretation of the references to colour in this figure legend, the reader is referred to the web version of this article.)

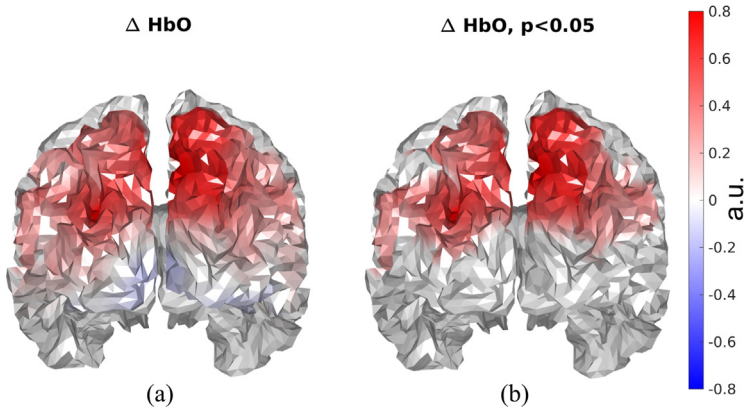

Fig. 6. Group average projection of ΔHbO onto the cortical surface. The amplitudes are normalized between -1 and 1. (a) Plain group average. (b) Only voxels with $p < 0.05$ are displayed. Notice the larger spatial spread in comparison to Fig. 3(a) and (c). The standard Colin27-based brain surface from Fieldtrip is used.

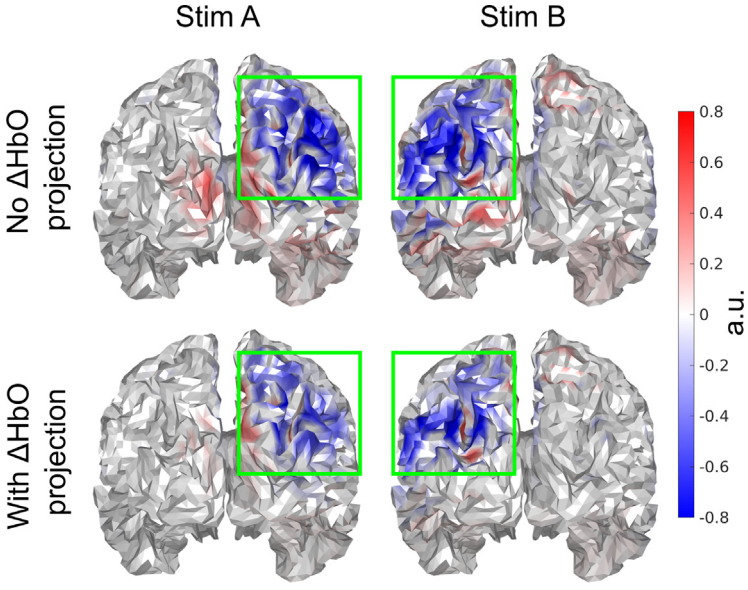

Fig. 7. Improved spatial confinement of source reconstruction at the respective N170 peaks when using ΔHbO as the spatial prior. Each subfigure was individually normalized between -1 and 1 for better clarity. Colorbars slightly saturated for better visualization. Only voxels with $p < 0.05$ are displayed. The standard Colin27-based brain surface from Fieldtrip is used.

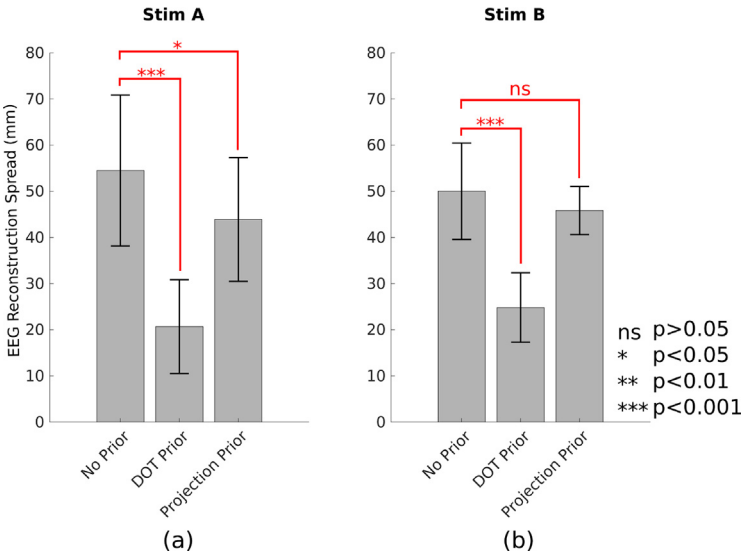

Fig. 8. Comparison of group level spread metric using no prior, DOT prior, and ΔHbO projection prior. Shown are group averages, standard deviations, as well as results of statistical testing for the two stimuli separately.

improved. We also showed that while ΔHbO projection prior can also improve the EEG reconstruction accuracy, it can be insufficient in reducing spatial spread.

While DOT does have the potential of achieving spatial resolutions that are comparable with fMRI, such setups typically require a very high-density optode grid (Eggebrecht et al., 2012), and when a lower-density grid is used, the resolution can be lower (albeit still higher than that of regular density EEG, as is shown in this work) and artifacts may arise (White and Culver, 2010b). Nevertheless, the fact that the relatively low-density DOT grid still led to a substantial improvement in the spatial accuracy of EEG reconstruction, both in simulation and experimental data, implies that the effectiveness of the algorithm is only underestimated, because the more accurate spatial priors derived from high-density DOT systems can potentially further improve the results.

Indeed, there exist DOT systems with sample rates up to 250 Hz (Scholkmann et al., 2014), which can theoretically distinguish between the two stimuli used in the experiment. However, the combination of EEG and DOT is still of value because it allows us to gain more information beyond mere distinguishability: the temporal evolution of neuronal activities in response to stimuli, e.g. the signal propagation shown in Fig. S4 and the Supplementary Videos. The fast neuronal dynamics cannot be resolved using only DOT due to the slow nature of the hemodynamics, and spatial accuracy can be lacking when using EEG alone.

In Section 2.5, we assumed the EEG sensor noise to be i.i.d. This is a commonly-made assumption in the field of EEG source reconstruction for better tractability, and good results have been obtained although the assumption may not always be satisfied (Grech et al., 2008; Henson et al., 2010; Luessi et al., 2011; Morioka et al., 2014). Although we made the conventional assumption in this paper, it is possible that if the noise profile of the EEG sensors (i.e. the covariance matrix) can be more accurately quantified, the results can be further improved, and it is straightforward to incorporate improved assumptions using our method.

Without having access to the individual structural MRI scans, we used a standard (Colin27) brain model for our data analyses, which can be another limiting factor of reconstruction accuracy. The asymmetry of the head model may also have contributed to the slightly asymmetric responses shown in Fig. 3. The effect of the incorporation of subject-specific structural scans should be investigated in future work.

In addition to the physical dimensions of the optode and electrode holders, another major factor that limits the density of the DOT grid is the size of the region of interest (ROI) and the typically small number of available optodes. In this paper, the locations of the optodes in both simulations and experiments were heuristically determined, and it is possible that an improved positioning of the optodes can further improve the results. There are some algorithms proposed to optimally place the optodes given an ROI (Brigadoi et al., 2018; Morais et al., 2018). However, such algorithms are optimized for spectroscopy (i.e. only sensor space analyses, but no source reconstruction) instead of tomography, and the optimal positioning of optodes for DOT applications still remains an open question and requires further investigation.

We made the simplifying assumptions that the neuronal activation and hemodynamic response are tightly coupled, in that neuronal activation should be strong if and only if the hemodynamic response is also strong, and vice versa. However, this may not hold if, e.g., one of the neuronal sources is not visible in the DOT reconstruction due to low signal-to-noise ratio, insufficient coverage of the grid, or too deep inside the brain such that DOT is not sensitive to it, etc. Further, the neuronal and hemodynamic activities may have altered coupling or even decoupling in certain diseases such as stroke and traumatic brain injury (Girouard and Iadecola, 2006). In these situations, caution must be used when applying the algorithm. One may tune the parameters in the ReML formulation (Section 2.5) to relax the constraints, or use the algorithm in conjunction with other robust algorithms that are specifically designed for mismatches in different modalities, such as Twomey (Liu et al., 2006). The algorithm should be further tested in diseased cases to better understand its limitations and potential improvements.

Although the improved spatial accuracy of EEG reconstruction using DOT prior shown using experimental data is highly promising, without having access to the ground truth, it is not fully known if such confinement is a result of over-constraining by the prior. This could be verified in future studies by incorporating recordings from other modalities i.e. fMRI, MEG that can possess higher volumetric spatial resolution than DOT (and EEG), potentially providing measurements closer to ground truth localization of neuronal and hemodynamic activity.

In conclusion, joint neuronal source reconstruction using simultaneous EEG and DOT shows great potential of being able to resolve neuronal activity with high spatio-temporal resolution. This can be of great benefit to both clinical applications and basic neuroscientific studies, e.g. localization of epileptic foci and understanding the information flow in the brain.

Funding

This work was supported by the National Science Foundation [NSF-CIF-1763561, NSF-STTR-2111735]; the Office of Naval Research [ONR N00014-19-1-1223]; and Carnegie Mellon Neuroscience Institute Presidential Fellowship.

Declaration of Competing Interest

None

Data availability

The data and scripts used to generate the results presented in this paper are available from the corresponding author for research purposes.

Acknowledgments

The authors would like to thank Andrew Levitsky, Audra Irvine, Deepshikha Acharya, and Alexander Rüsch for their generous help with the experiment design and setup.

Supplementary material

Supplementary material associated with this article can be found, in the online version, at 10.1016/j.neuroimage.2023.120210.

References

Abdelnour, F., Genovese, C., Huppert, T., 2010. Hierarchical Bayesian regularization of reconstructions for diffuse optical tomography using multiple priors. Biomed. Opt. Express 1 (4), 1084–1103. doi:10.1364/BOE.1.001084.

Aihara, T., Takeda, Y., Takeda, K., Yasuda, W., Sato, T., Otaka, Y., Hanakawa, T., Honda, M., Liu, M., Kawato, M., et al., 2012. Cortical current source estimation from electroencephalography in combination with near-infrared spectroscopy as a hierarchical prior. Neuroimage 59 (4), 4006–4021.

Ayaz, H., Baker, W.B., Blaney, G., Boas, D.A., Bortfeld, H., Brady, K., Brake, J., Brigadoi, S., Buckley, E.M., Carp, S.A., Cooper, R.J., Cowdrick, K.R., Culver, J.P., Dan, I., Dehghani, H., Devor, A., Durduran, T., Eggebrecht, A.T., Emberson, L.L., Fang, Q., Fantini, S., Franceschini, M.A., Fischer, J.B., Gervain, J., Hirsch, J., Hong, K.-S., Horstmeyer, R., Kainerstorfer, J.M., Ko, T.S., Licht, D.J., Liebert, A., Luke, R., Lynch, J.M., Mesquida, J., Mesquita, R.C., Naseer, N., Novi, S.L., Orihuela-Espina, F., O'Sullivan, T.D., Peterka, D.S., Pifferi, A., Pollonini, L., Sassaroli, A., Sato, J.a.R., Scholkmann, F., Spinelli, L., Srinivasan, V.J., Lawrence, K.S., Tachtsidis, I., Tong, Y., Torricelli, A., Urner, T., Wabnitz, H., Wolf, M., Wolf, U., Xu, S., Yang, C., Yodh, A.G., Yücel, M.A., Zhou, W., 2022. Optical imaging and spectroscopy for the study of the human brain: status report. Neurophotonics 9 (S2), S24001.

Barker, J.W., Aarabi, A., Huppert, T.J., 2013. Autoregressive model based algorithm for correcting motion and serially correlated errors in fNIRS. Biomed. Opt. Express 4 (8), 1366–1379.

Brigadoi, S., Salvagnin, D., Fischetti, M., Cooper, R.J., 2018. Array designer: automated optimized array design for functional near-infrared spectroscopy. Neurophotonics 5 (3), 035010.

Cao, J., Huppert, T.J., Grover, P., Kainerstorfer, J.M., 2021. Enhanced spatiotemporal resolution imaging of neuronal activity using joint electroencephalography and diffuse optical tomography. Neurophotonics 8 (1), 015002.

Dehghani, H., Eames, M.E., Yalavarthy, P.K., Davis, S.C., Srinivasan, S., Carpenter, C.M., Pogue, B.W., Paulsen, K.D., 2009. Near infrared optical tomography using NIRFAST: algorithm for numerical model and image reconstruction. Commun. Numer. Methods Eng. 25 (6), 711–732.

Eggebrecht, A.T., Ferradal, S.L., Robichaux-Viehoever, A., Hassanpour, M.S., Dehghani, H., Snyder, A.Z., Hershey, T., Culver, J.P., 2014. Mapping distributed brain function and networks with diffuse optical tomography. Nat. Photonics 8 (6), 448–454.

Eggebrecht, A.T., White, B.R., Ferradal, S.L., Chen, C., Zhan, Y., Snyder, A.Z., Dehghani, H., Culver, J.P., 2012. A quantitative spatial comparison of high-density diffuse optical tomography and fMRI cortical mapping. Neuroimage 61 (4), 1120–1128.

Fang, Q., Boas, D.A., 2009. Tetrahedral mesh generation from volumetric binary and grayscale images. In: IEEE International Symposium on Biomedical Imaging: From Nano to Macro, 2009. ISBI'09. Ieee, pp. 1142–1145.

Ferdowsi, S., Abolghasemi, V., Sanei, S., 2015. A new informed tensor factorization approach to EEG–fMRI fusion. J. Neurosci. Methods 254, 27–35.

Ferradal, S.L., Eggebrecht, A.T., Hassanpour, M., Snyder, A.Z., Culver, J.P., 2014. Atlas-based head modeling and spatial normalization for high-density diffuse optical tomography: in vivo validation against fMRI. Neuroimage 85, 117–126.

Fishburn, F.A., Ludlum, R.S., Vaidya, C.J., Medvedev, A.V., 2019. Temporal derivative distribution repair (TDDR): a motion correction method for fNIRS. Neuroimage 184, 171–179.

Girouard, H., Iadecola, C., 2006. Neurovascular coupling in the normal brain and in hypertension, stroke, and Alzheimer disease. J. Appl. Physiol. 100 (1), 328–335.

Grech, R., Cassar, T., Muscat, J., Camilleri, K.P., Fabri, S.G., Zervakis, M., Xanthopoulos, P., Sakkalis, V., Vanrumste, B., 2008. Review on solving the inverse problem in EEG source analysis. J. Neuroeng. Rehabil. 5 (1), 1–33.

Grover, P., Venkatesh, P., 2017. An information-theoretic view of EEG sensing. Proc. IEEE 105 (2), 367–384.

Henson, R.N., Flandin, G., Friston, K.J., Mattout, J., 2010. A parametric empirical Bayesian framework for fMRI-constrained MEG/EEG source reconstruction. Hum. Brain Mapp. 31 (10), 1512–1531.

Keles, H.O., Barbour, R.L., Omurtag, A., 2016. Hemodynamic correlates of spontaneous neural activity measured by human whole-head resting state EEG+ fNIRS. Neuroimage 138, 76–87.

Liu, Z., He, B., 2008. fMRI-EEG integrated cortical source imaging by use of time-variant spatial constraints. Neuroimage 39 (3), 1198–1214.

Liu, Z., Kecman, F., He, B., 2006. Effects of fMRI-EEG mismatches in cortical current density estimation integrating fMRI and EEG: a simulation study. Clin. Neurophysiol. 117 (7), 1610–1622.

Luessi, M., Babacan, S.D., Molina, R., Booth, J.R., Katsaggelos, A.K., 2011. Bayesian symmetrical EEG/fMRI fusion with spatially adaptive priors. Neuroimage 55 (1), 113–132.

Michel, C.M., He, B., 2019. EEG source localization. Handb. Clin. Neurol. 160, 85–101.

Morais, G.A.Z., Balardin, J.B., Sato, J.a.R., 2018. fNIRS optodes location decider (fOLD): a toolbox for probe arrangement guided by brain regions-of-interest. Sci. Rep. 8 (1), 1–11.

Morioka, H., Kanemura, A., Morimoto, S., Yoshioka, T., Oba, S., Kawanabe, M., Ishii, S., 2014. Decoding spatial attention by using cortical currents estimated from electroencephalography with near-infrared spectroscopy prior information. Neuroimage 90, 128–139.

Oberlin, T., Barillot, C., Gribonval, R., Maurel, P., 2015. Symmetrical EEG-fMRI imaging by sparse regularization. In: 2015 23rd European Signal Processing Conference (EUSIPCO). IEEE, pp. 1870–1874.

Oostenveld, R., Fries, P., Maris, E., Schoffelen, J.-M., 2011. FieldTrip: open source software for advanced analysis of MEG, EEG, and invasive electrophysiological data. Comput Intell Neurosci 2011, 1.

Oostenveld, R., Praamstra, P., 2001. The five percent electrode system for high-resolution EEG and ERP measurements. Clin. Neurophysiol. 112 (4), 713–719.

Oostenveld, R., Stegeman, D.F., Praamstra, P., van Oosterom, A., 2003. Brain symmetry and topographic analysis of lateralized event-related potentials. Clin. Neurophysiol. 114 (7), 1194–1202.

Rolls, E.T., Huang, C.-C., Lin, C.-P., Feng, J., Joliot, M., 2020. Automated anatomical labelling atlas 3. Neuroimage 206, 116189.

Santosa, H., Zhai, X., Fishburn, F., Huppert, T., 2018. The NIRS brain AnalyzIR toolbox. Algorithms 11 (5), 73.

Scholkmann, F., Kleiser, S., Metz, A.J., Zimmermann, R., Pavia, J.M., Wolf, U., Wolf, M., 2014. A review on continuous wave functional near-infrared spectroscopy and imaging instrumentation and methodology. Neuroimage 85, 6–27.

White, B.R., Culver, J.P., 2010. Phase-encoded retinotopy as an evaluation of diffuse optical neuroimaging. Neuroimage 49 (1), 568–577.

White, B.R., Culver, J.P., 2010. Quantitative evaluation of high-density diffuse optical tomography: in vivo resolution and mapping performance. J. Biomed. Opt. 15 (2), 026006.

Zeff, B.W., White, B.R., Dehghani, H., Schlaggar, B.L., Culver, J.P., 2007. Retinotopic mapping of adult human visual cortex with high-density diffuse optical tomography. Proc. Natl. Acad. Sci. 104 (29), 12169–12174.